



In-situ one-step synthesis of novel BiOCl/Bi₂₄O₃₁Cl₁₀ heterojunctions via self-combustion of ionic liquid with enhanced visible-light photocatalytic activities



Fa-tang Li^{a,*}, Qing Wang^a, Xiao-jing Wang^a, Bo Li^b, Ying-juan Hao^a, Rui-hong Liu^a, Di-shun Zhao^c

^a College of Science, Hebei University of Science and Technology, Shijiazhuang, China

^b Analytical & Testing Center of Hebei Province, Hebei University of Science and Technology, Shijiazhuang, China

^c College of Chemical and Pharmaceutical Engineering, Hebei University of Science and Technology, Shijiazhuang, China

ARTICLE INFO

Article history:

Received 8 October 2013

Received in revised form 2 January 2014

Accepted 4 January 2014

Available online 10 January 2014

Keywords:

BiOCl/Bi₂₄O₃₁Cl₁₀ heterojunction

Ionic liquid

Combustion synthesis

Photocatalysis

Visible light

ABSTRACT

A facile and fast method was developed for the preparation of novel BiOCl/Bi₂₄O₃₁Cl₁₀ heterojunctions via a self-combustion of ionic liquids (ILs) route. The ILs were prepared from Bi(NO₃)₃·5H₂O and diethylamine hydrochloride ((C₂H₅)₂NH·HCl). The photocatalysts were obtained by heating the ILs to combustion. In the ILs system, (C₂H₅)₂NH·HCl serves not only as the source of cation in IL, but also as the main fuel. The prepared composites exhibit noticeable visible light photocatalytic activity in the degradation of organic pollutants, including anionic dye methyl orange and cationic dye rhodamine B, which is attributed to the narrow band gap (2.3 eV) and the effective electrons transfer from the conductive band of Bi₂₄O₃₁Cl₁₀ to that of BiOCl, improving the separation efficiency of the photo-generated electron/hole pairs. The heterojunction containing 60.4% BiOCl and 39.6% Bi₂₄O₃₁Cl₁₀ exhibits the highest photocatalytic activity. The heterojunction shows dramatic adsorption performance for cationic dye rhodamine B because of its surface negative charges. The radical scavengers result shows that hole is the main reactive species responsible for the degradation of pollutants and superoxide radicals are also involved in the photocatalytic process. The results obtained may provide a new sight for broadening the application of ILs in the preparation of nanomaterials and for the in-situ one-step synthesis of heterostructural materials.

© 2014 Elsevier B.V. All rights reserved.

1. Introduction

Photocatalysis has attracted increasing attention as a potential green technology to decompose organic pollutants into inorganic substances for environmental purification, to split water into hydrogen and oxygen gases and to reduce CO₂ for clean energy production, as well as to synthesize organic reagents over the last few decades [1–4]. To date, TiO₂ is the most widely studied semiconductor for photocatalysis due to its high photoactivity, low cost, chemical and photochemical stability, non-toxicity, and environmentally friendly features [5,6]. However, the rapid recombination rate of the photogenerated electrons and holes on the surface and in the bulk phase of the TiO₂ leads to a low quantum yield [7–9], and the photocatalytic activity of TiO₂ under visible light is extremely low due to its wide band gap (3.0–3.2 eV) [10]. Thus, the two main drawbacks hinder its practical applications.

To improve the application efficiency of TiO₂ in visible light region, many strategies have been employed, such as metal or nonmetal elements doping [11], noble metal deposition [12], surface functionalization [13], combination of semiconductor photocatalysts [7]. Besides these, exploiting novel photocatalysts capable of absorbing visible light is an effective approach [10].

In recent years, BiOCl has drawn considerable interest due to its good photocatalytic activity under UV irradiation [1,14–18] since Zhang et al. confirmed that its efficiency in photodegradation of methyl orange was higher than commercial P25 TiO₂ [1]. The high activity of BiOCl can be attributed to its unique layer structure, which is characterized by [Bi₂O₂]²⁺ slabs interleaved by double slabs of Cl atoms with an internal static electric field that is perpendicular to each layer [19]. This structure can efficiently favor the transfer of electrons and holes generated inside the crystal surface and promote the electrons/holes separation, enhancing quantum yield [20]. However, BiOCl with a wide band gap (3.19–3.60 eV, related to its preparation methods and morphologies) can only absorb ultraviolet light, which is similar to TiO₂ and is also limited for efficient utilization of solar energy [21].

* Corresponding author. Tel.: +86 311 81669971; fax: +86 311 81668528.
E-mail address: lifatang@126.com (F.-t. Li).

To utilize the high quantum efficiency of BiOCl under visible light irradiation, an efficient strategy is combining BiOCl with narrow band gap semiconductors to form heterojunction [10,20–26]. The heterojunctions composed by two photocatalysts with suitable CB and VB levels can efficiently reduce the recombination of photoinduced electron–hole pairs to increase the lifetime of charge carriers. So far, variety of heterojunctions systems, including BiOCl/bismuth oxyhydrate (BHO) [10], BiOI/BiOCl [19,20], Bi₂S₃/BiOCl [21,22], BiOCl/Bi₂O₃ [23], WO₃/BiOCl [24], NaBiO₃/BiOCl [25], and BiOCl/BiOBr [26] etc. were reported. These coupled semiconductors have displayed much higher visible light photocatalytic activities than individual photocatalysts in degradation of organic pollutants.

To prepare heterojunction composites, many methods have been employed, such as solvothermal method [10,19,26], hydrolysis and ions change [20], in situ reaction with HCl [23], and wet impregnation [24]. Compared to these techniques, solution combustion synthesis (SCS) is both energy- and time-efficient. Furthermore, in this process, copious gas evolves during the combustion process, resulting in a finely dispersed and porous morphology for the synthesized product, which is benefit to the adsorption of the pollutants on the catalysts [27]. Many oxide semiconductors, including TiO₂, ZnO, SnO₂, BiVO₄, and LaFeO₃ have been synthesized via SCS [27,28]. SCS is also used to prepare nanocomposites with hybrid structure, such as ZnO/Fe₂O₃ [29]. We also obtained α - and β -Fe₂O₃ mixed-phase by the self-combustion of ionic liquid (IL) [30] and TiO₂/amorphous Al₂O₃ composite by SCS [7]. So, can BiOCl-based hybrid materials be prepared by this simple and fast technique?

Bi₂₄O₃₁Cl₁₀ is a product of the thermal decomposition of BiOCl [31]. It has a narrow energy band gap of ca. 2.90 eV, corresponding to a visible light absorption wavelength of 427 nm. If it has a suitable CB and VB levels for BiOCl, Bi₂₄O₃₁Cl₁₀/BiOCl heterojunction may be an efficient photocatalyst in visible light region.

In the present study, Bi₂₄O₃₁Cl₁₀/BiOCl heterojunctions have been prepared via the self-combustion of ILs. Herein, ILs were prepared from Bi(NO₃)₃ and diethylamine hydrochloride ((C₂H₅)₂NH·HCl), which were stable liquid systems. (C₂H₅)₂NH·HCl not only provides the cation for IL, but also serves as the main fuel for combustion. Homogeneity is achieved primarily because the IL is mixed on an atomic scale, which ensures the formation of nanopowders. The ratio of Bi₂₄O₃₁Cl₁₀ to BiOCl can be adjusted by varying the ratio of (C₂H₅)₂NH·HCl to urea, which serves as assistant fuel. Furthermore, the new composite materials showed extraordinary photocatalytic activities in degradation of methylene orange (MO) and rhodamine B (RhB). The photocatalytic mechanism of heterojunctions with enhanced activities was also proposed.

2. Experimental

2.1. Catalysts preparation

All chemicals were procured from Aladdin and used as received. To prepare various photocatalysts, 0.01 mol Bi(NO₃)₃·5H₂O was mixed with 0.052 to 0.01 mol of (C₂H₅)₂NH·HCl and 0 or 0.005 mol of urea (assistant fuel). The mixtures were heated on an electric furnace until homogeneous white solutions were formed. After being cooled to room temperature, the solutions still remained liquid status, owing to the formation of their ionic liquid structure. Then the solutions were transferred into a tube furnace, in which the solutions were heated continuously up to 300 °C for 3 min with a heating rate of 10 °C/min and O₂ flow rate of 500 mL/min. Finally, the products were obtained and taken out from the furnace to be used for experiments and characterized.

2.2. Material characterization and analysis

X-ray diffraction (XRD) was used to characterize the phases composition and ratios of obtained samples with a Rigaku D/MAX 2500 X-ray diffractometer. The morphologies of as-prepared photocatalysts were characterized by field-emission scanning electron microscope (FE-SEM, FEI XL 30 ESEM FEG). Transmission electron microscopy (TEM) and high-resolution electron microscopy (HREM) images were taken using a JEOL JEM-2010 electron microscope. The UV–vis diffuse reflectance spectra (DRS) were acquired between 200 and 800 nm using a Thermo Scientific Evolution 220 spectrophotometer to observe their optical properties. BET specific surface areas of the samples were measured with a Quantachrome NOVA2000 nitrogen adsorption/desorption apparatus. The surface charge of BiOCl–Bi₂₄O₃₁Cl₁₀ particles in aqueous solution was obtained using a zeta-potential analyser (Malvern Zetasizer Nano-ZS 90). The surface photovoltage (SPV) measurements were carried out with a homemade apparatus (a 500 W Xe lamp).

2.3. Photocatalytic activities test

MO, RhB, and 4-chlorophenol (4-CP) were used as anionic dye, cationic dye, and colorless target pollutant, respectively, to evaluate the photocatalytic activity of the photocatalysts. The photocatalytic reaction was conducted using a 350-W Xe lamp equipped with a 400 nm cut-off filter as the visible light source. The total light intensity was 0.48 W/cm² in the range of 400–1064 nm measured by a Newport 842-PE optical power/energy meter. In each experiment, 0.10 g of the catalyst was added to 100 mL of an aqueous solution that contained 10 mg/L of pollutants. Prior to illumination, the suspensions were continuously stirred in the dark for 30 min to reach the adsorption/desorption equilibrium of the dyes on the surface of photocatalysts. At given time intervals, 5 mL of the suspension was withdrawn, centrifuged, and filtered to remove the photocatalysts. Then the maximum absorption wavelengths varying with the reaction time were taken to test the concentration of MO and RhB using a Thermo Scientific Evolution 220 UV–vis spectrophotometer. The concentration of 4-CP was determined by measuring the absorbance at 225 nm on UV–vis spectrophotometer. The decoloration efficiency was reported as C/C_0 , where C is the pollutants concentration after adsorption or photocatalysis, and C_0 is the initial concentration of 10 mg/L. To investigate the stability of the used photocatalyst, the nanopowders were separated from solution by centrifugation at 13,000 r/min for 4 min, then dried in drying oven at 120 °C for 2 h and used for the next run experiment.

2.4. Determination of reactive species

To detect the possible reactive species involved in the photocatalytic process, various scavengers, including isopropanol (*t*-BuOH, 10 m mol/L), AgNO₃ (6 m mol/L), ammonium oxalate monohydrate (((NH₄)₂C₂O₄·H₂O, 1 m mol/L), N₂ (0.2 L/min) were introduced into the solution of RhB. Nitrotetrazolium blue chloride (NBT, 2.5×10^{-5} mol/L) was used to observe the amount of $\bullet\text{O}_2^-$ generated in the photocatalytic process because NBT can exhibit a maximum absorption peak at 260 nm while the product of $\bullet\text{O}_2^-$ and NBT don't [32]. The experimental procedures were as follows: NBT was dissolved in H₂O to form a 2.5×10^{-5} mol/L solution. Then, 0.10 g of the photocatalyst was dispersed in 100 mL of the NBT aqueous solution. The suspension was irradiated under visible light and 5 mL of sample was sampled, centrifuged, filtered, and measured on Shimadzu UV-2550 spectrophotometer every 20 min. Meanwhile, the relative concentration of $\bullet\text{OH}$ radicals was estimated by terephthalic acid (TA) fluorescence method because TA can react with $\bullet\text{OH}$ radicals to form high fluorescent 2-hydroxyterephthalic acid

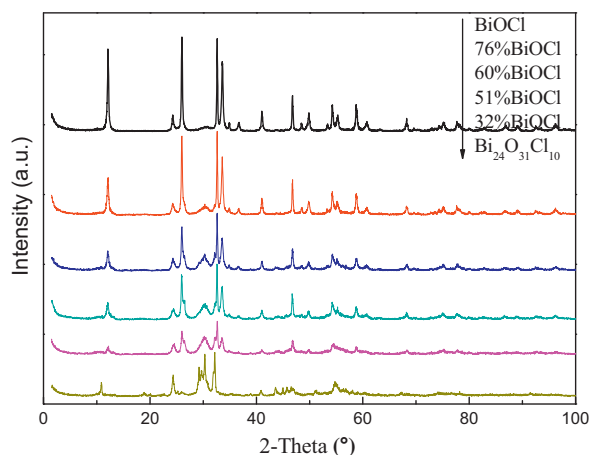


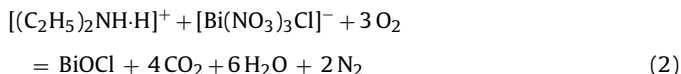
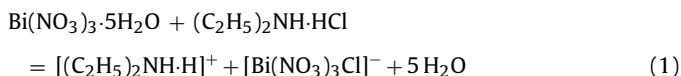
Fig. 1. XRD patterns of (a) pure BiOCl; (b) 76%BiOCl; (c) 60%BiOCl; (d) 51%BiOCl; (e) 32%BiOCl; and (f) pure Bi₂₄O₃₁Cl₁₀.

(TAOH) [33,34]. To observe fluorescence spectra, TA was dissolved in 2.0 mM NaOH to form a solution with a concentration of 0.5 mM. Then, 0.1 g of the photocatalyst was added to 100 mL of the solution, and the mixture was irradiated under visible light and measured on a Hitachi F-4600 fluorescence spectrophotometer (excited wavelength: 315 nm). To detect generation of activated species, electron spin resonance (ESR) signals of radicals spin-trapped by 5,5-dimethyl-1-pyrroline-*N*-oxide (DMPO) was collected on a Bruker EMX-8/2.7 X-band ESR spectrometer operating in the X-band at 9.86 GHz under visible light irradiation ($\lambda > 400$ nm).

3. Results and discussion

3.1. Structural and morphological characterization

After many times calcination experiments, we found that when 0.01 mol of Bi(NO₃)₃·5H₂O was mixed with equal molar of (C₂H₅)₂NH·HCl and then the mixture was heated following the procedure listed in Section 2.1, the obtained powders exhibited pure and highly crystalline BiOCl phase (JCPDS NO. 01-082-0485), without other impurities or undecomposed reactants, as shown in Fig. 1. The formation of ionic liquid and product are estimated as following equations:



In our previous works [28,30], mixed-phase Fe₂O₃ and LaFeO₃ have been prepared successfully via the self-combustion of ILs. In this study, similar to previous systems, the homogeneity of the ionic liquids $[(\text{C}_2\text{H}_5)_2\text{NH} \cdot \text{H}]^+[\text{Bi}(\text{NO}_3)_3\text{Cl}]^-$ ensures the formation of products with nanostructures.

Compared to BiOCl, Bi₂₄O₃₁Cl₁₀ contains more O and less Cl atoms. To synthesize BiOCl/Bi₂₄O₃₁Cl₁₀ composites, less (C₂H₅)₂NH·HCl containing Cl element was used to adjust the ratio of BiOCl and Bi₂₄O₃₁Cl₁₀. The samples obtained from various fuels amount are denoted in Table 1.

Fig. 1 shows the XRD patterns of the as-synthesized samples. It is seen that the sample prepared with the molar ratio of

Bi(NO₃)₃:ethanamine:urea = 1:0.52:0.5 exhibits a pure Bi₂₄O₃₁Cl₁₀ phase (JCPDS NO. 01-075-0887). When the ethanamine amount was changed from 0.0062 to 0.0082 while that of Bi(NO₃)₃ and urea was fixed 0.01 and 0.005 mol, respectively, the peaks of the samples exhibit a coexistence of both BiOCl and Bi₂₄O₃₁Cl₁₀ phases. It can be also observed from Fig. 1 that, with the decrease of the ethanamine, the intensities of diffraction peaks of Bi₂₄O₃₁Cl₁₀ increase continuously whereas those of BiOCl decrease simultaneously. This indicates that ethanamine plays an important role in the formation of BiOCl and Bi₂₄O₃₁Cl₁₀.

To calculate the phase composition quantitatively, RIR method is employed. The weight ratio of each composition in the hetero-materials can be calculated using the following formula [35]:

$$W_a = \frac{I_a}{I_a + (I_b/RIR_b/RIR_a)}$$

$$W_b = \frac{I_b}{I_b + (I_a/RIR_a/RIR_b)} = 1 - W_a$$

According to the RIR values of BiOCl and Bi₂₄O₃₁Cl₁₀ phase read from the PDF database, which are 9.69 and 7.67, respectively, the calculated weight ratios of BiOCl/Bi₂₄O₃₁Cl₁₀ heterostructures are listed in Table 1. In the calculation process, the “WPF Refinement” function of the “MDI JADE 6.5” software was employed.

Fig. 2 shows the SEM images of various samples. The image in Fig. 2a displays that the pure BiOCl sample is mainly consisted of irregular plates, which are 0.2–1.0 μm in width and ca. 20 nm in thickness. Fig. 2e reveals that pure Bi₂₄O₃₁Cl₁₀ exhibits sheet structure. It is also seen that Bi₂₄O₃₁Cl₁₀ has smaller particles than BiOCl. Figs. 2b to d exhibit the morphology of different BiOCl/Bi₂₄O₃₁Cl₁₀ heterostructures. There are plates and nanopowders in the images, showing the coexistence of BiOCl and Bi₂₄O₃₁Cl₁₀. It is also seen that with the increase of Bi₂₄O₃₁Cl₁₀, the plate-shaped sample decreases and the smaller particles increase. The BET specific surface areas of various samples are listed in Table 1. The results show that with the decrease of the fuel of (C₂H₅)₂NH·HCl, the surface area increases. The reason is less fuel resulted in more Bi₂₄O₃₁Cl₁₀ in the heterojunction, which has a higher surface area than BiOCl. The results are consistent with the SEM images.

Fig. 3a shows the TEM image with two different parts of 60%BiOCl/Bi₂₄O₃₁Cl₁₀ heterojunction. The grey region with flake shape is the image of BiOCl with layer structure. It is also seen that there is also a porous structure, which is caused by the release of the massive gas during the combustion process. The other part with dark color is the reflection of Bi₂₄O₃₁Cl₁₀. The morphology obtained from TEM is consistent with the SEM result. To further observe the structure information of the hybrid material, the HRTEM image is shown in Fig. 3b. It is seen that there are two mixed fringes with *d* values of 0.275 and 0.306 nm, corresponding to the (1 1 0) plane of BiOCl and (3 0 4) plane of Bi₂₄O₃₁Cl₁₀, respectively. The image indicates clearly the presence of the mixed phase of BiOCl and Bi₂₄O₃₁Cl₁₀.

3.2. Optical properties

The energy band gap of a semiconductor is closely related to its photoabsorption and photocatalytic ability. Fig. 4a shows the UV–vis diffuse absorption spectra of the as-prepared samples with different BiOCl contents. It is seen that pure BiOCl has almost no absorption in the visible light range with an absorption edge at around 365 nm, whereas pure Bi₂₄O₃₁Cl₁₀ has strong absorption in the visible light region with an absorption edge about 490 nm. It is also found BiOCl/Bi₂₄O₃₁Cl₁₀ heterostructures have prominent absorption in the visible light region, and their absorption edges shift monotonically to longer wavelengths with increased Bi₂₄O₃₁Cl₁₀ contents. The maximum absorption wavelengths of

Table 1

Phase composition, surface area and band gap of the as-prepared samples obtained from different fuels.

Sample	Molar ratio of Bi(NO ₃) ₃ :ethanamine:urea	Phase composition (wt%)		BET surface area (m ² g ⁻¹)	Band gap (eV)
		BiOCl	Bi ₂₄ O ₃₁ Cl ₁₀		
BiOCl	1:1:0	100	0	2.13	3.20
76%BiOCl	1:0.82:0.5	76.9	23.1	2.56	2.54
60%BiOCl	1:0.76:0.5	60.4	39.6	3.07	2.41
51%BiOCl	1:0.70:0.5	51.0	49.0	3.29	2.39
32%BiOCl	1:0.62:0.5	32.3	67.7	3.59	2.38
Bi ₂₄ O ₃₁ Cl ₁₀	1:0.52:0.5	0	100	4.03	2.30

BiOCl/Bi₂₄O₃₁Cl₁₀ composites with 76%, 60%, 51%, and 32% BiOCl are 420, 450, 483, and 486 nm, respectively. The UV–vis spectra result is in accordance with the color of the as-prepared samples changing from white to yellow, as shown in Fig. 4b.

The band gap energy of a semiconductor can be evaluated by the following equation [36]: $\alpha(h\nu) = a(h\nu - E_g)^{n/2}$, where α , h , ν , A , and E_g represent the absorption coefficient, Planck's constant, light frequency, energy-independent constant, and band gap, respectively. The value of n is a constant that depends on the characteristics of the transition in the semiconductor, including direct transition ($n = 1$) and indirect transition ($n = 4$). For BiOX, n is 4 for their indirect transition [19]. Based on the equation, the band gaps of the samples can be deduced from the tangent line that are extrapolated

to $(\alpha(h\nu))^{1/2} = 0$, which is shown in Fig. 4c and the band gaps of various samples obtained are listed in Table 1. The results indicate that, except for pure BiOCl, all the heterostructures can absorb visible light and can be used as potential photocatalysts under visible light irradiation.

3.3. Photocatalytic properties

The photocatalytic performances of the as-prepared samples were evaluated with respect to the degradation of MO as the model pollutant firstly under visible light irradiation. Fig. 5a presents the variation of MO concentration (C/C_0) as the function of reaction time. It is seen that there is about 3.0% MO degradation in

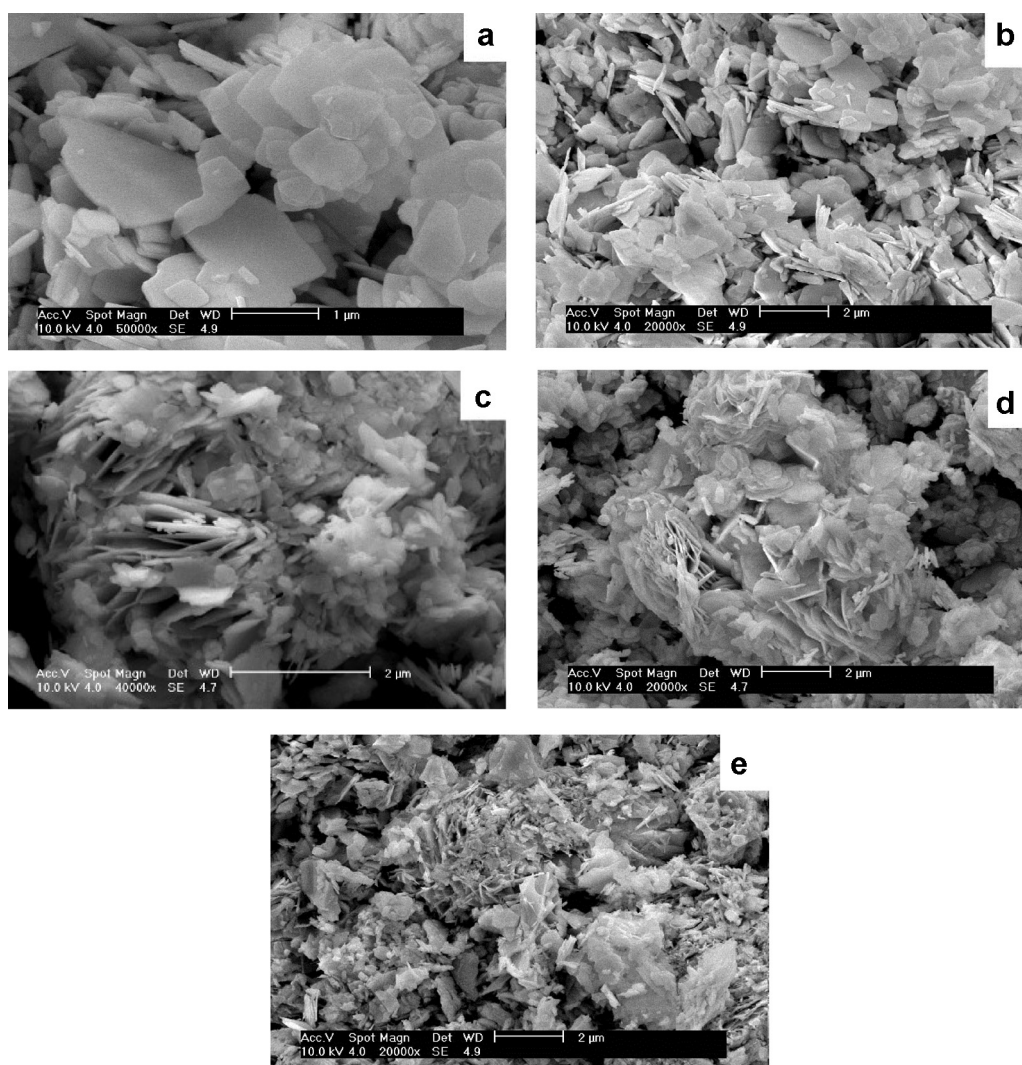


Fig. 2. FESEM images of samples (a) BiOCl, (b) 76%BiOCl; (c) 60%BiOCl; (d) 32%BiOCl; and (e) pure Bi₂₄O₃₁Cl₁₀.

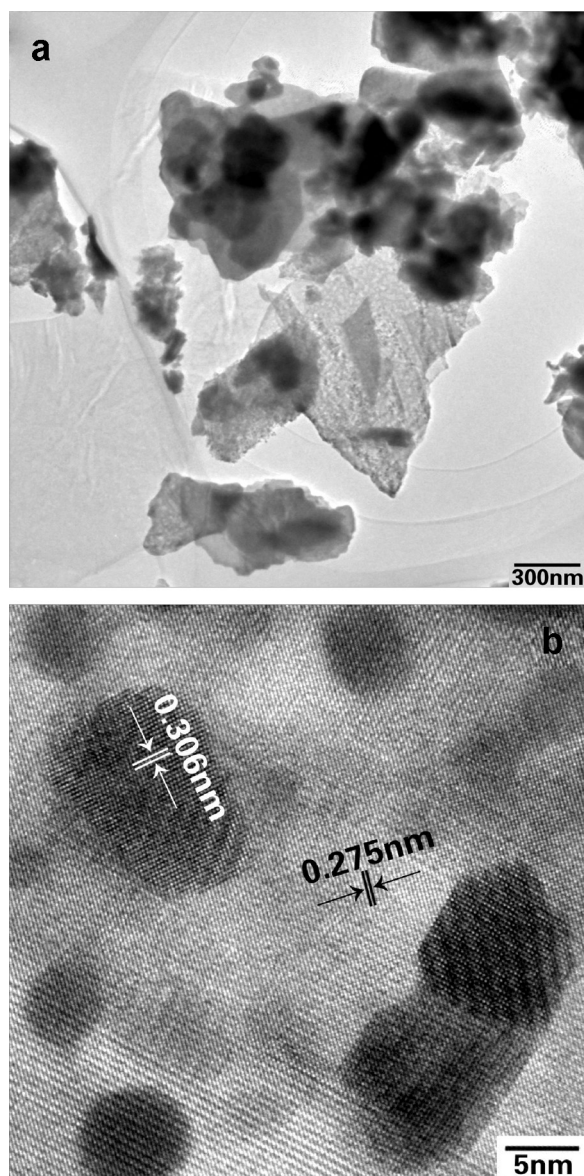


Fig. 3. (a) TEM and (b) HRTEM images of 60%BiOCl heterojunction.

the absence of photocatalyst at the same conditions from a blank experiment, indicating that the self-photolysis of MO is very limited and can be negligible. For comparison, P25 TiO₂ was used as reference. It is known that P25 can only absorb ultraviolet light and has no visible light photocatalytic activity. As shown in Fig. 5a, the degradation efficiency of MO with P25 is similar to its self-photolysis, implying there is no photosensitization effect for MO over P25 TiO₂. It is also seen that except for adsorption, there is a very slowly degradation tendency over pure BiOCl, showing BiOCl is not an effective photocatalyst under visible light. As to Bi₂₄O₃₁Cl₁₀, 30.3% MO is decolorized after 30 min of adsorption and 90 min of irradiation, indicating that it has certain photocatalytic ability under visible light irradiation. However, its degradation efficiency is limited maybe because of its fast recombination rate of photoinduced carriers. As comparison, there is a steady and continuous degradation of MO over the as-prepared heterojunctions. After 90 min of irradiation, the photodegradation efficiencies of MO are 35.3%, 74.5%, 53.2%, and 54.8% with 76%BiOCl, 60%BiOCl, 51%BiOCl, and 32%BiOCl, respectively. The 60%BiOCl shows the highest photocatalytic ability.

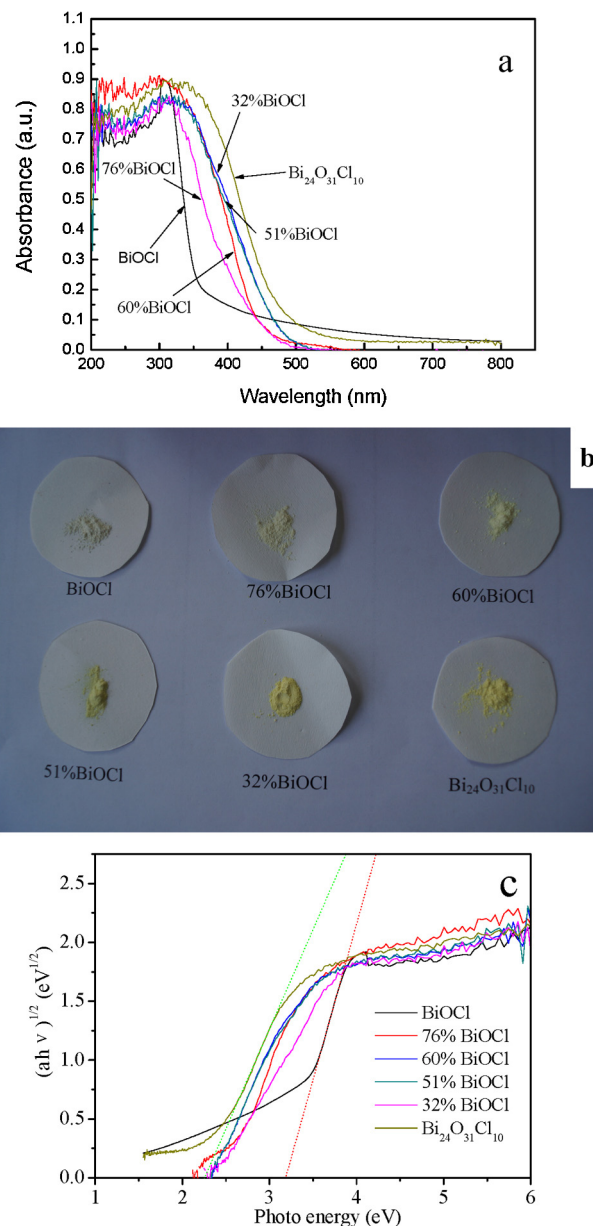


Fig. 4. (a) UV-vis diffuse reflectance spectra of BiOCl, Bi₂₄O₃₁Cl₁₀, and BiOCl/Bi₂₄O₃₁Cl₁₀ heterostructures; (b) appearance photographs of the samples; and (c) plots of $(\alpha(h\nu))^{1/2}$ versus energy ($h\nu$) for the band gap energies of various photocatalysts.

To further understand the reaction kinetics of MO degradation and to quantitative compare the photocatalytic abilities of various catalysts, the apparent pseudo-first-order model expressed by following equation is employed [7]:

$$\ln \frac{C_0}{C_t} = kt + \ln \frac{C_0}{C_1}$$

where k is the pseudo-first-order rate constant, C_0 is the original MO concentration (10 mg/L), C_1 is the concentration after adsorption, and C_t is the concentration at reaction time t . Fig. 5b shows the time-course variation of $\ln(C_0/C)$. The fitting curves for the experiment data are coerced to go through the intercepts of $\ln(C_0/C_1)$ in the y-axis, which are 0.0677, 0.0557, 0.0618, 0.0786, 0.0572, 0.0158, and 0.0423 for pure BiOCl, 76%BiOCl, 60%BiOCl, 51%BiOCl, 32%BiOCl, pure Bi₂₄O₃₁Cl₁₀, and P25 TiO₂, respectively. These values reflect the adsorption efficiency of photocatalysts for the MO molecules,

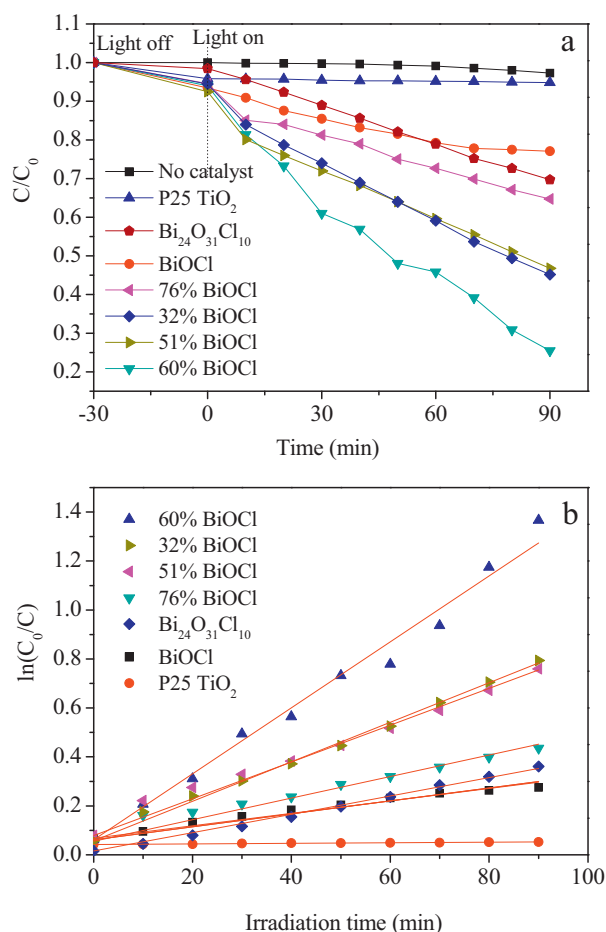


Fig. 5. Time-course variation of (a) C/C_0 and (b) $\ln(C_0/C)$ of MO solution under visible light illumination over various catalysts.

which is related to the surface area, surface property and morphology etc. The calculated k and correlation coefficient R are listed in Table 2. It is seen that the k values of heterojunctions 60%BiOCl, 51%BiOCl, and 32%BiOCl are higher than those of single BiOCl and $\text{Bi}_{24}\text{O}_{31}\text{Cl}_{10}$, which shows that the BiOCl/ $\text{Bi}_{24}\text{O}_{31}\text{Cl}_{10}$ heterojunction composites can be used as effective photocatalysts in visible light region. The reason that 76%BiOCl exhibits lower activity than that of $\text{Bi}_{24}\text{O}_{31}\text{Cl}_{10}$ may be attributed to its less $\text{Bi}_{24}\text{O}_{31}\text{Cl}_{10}$ content, which is responsible for the absorbance of visible light.

It is known that MO with a sulphuric group is a kind of anionic dyes. To investigate the universal of the as-prepared photocatalysts for various dyes, RhB was selected as a cationic dye for degradation. The time-course variation of C/C_0 and $\ln(C_0/C)$ of RhB are shown in Fig. 6a and b, respectively. The pseudo-first-order kinetics equations are calculated and the results are shown in Table 3. It can be seen that there are some difference between

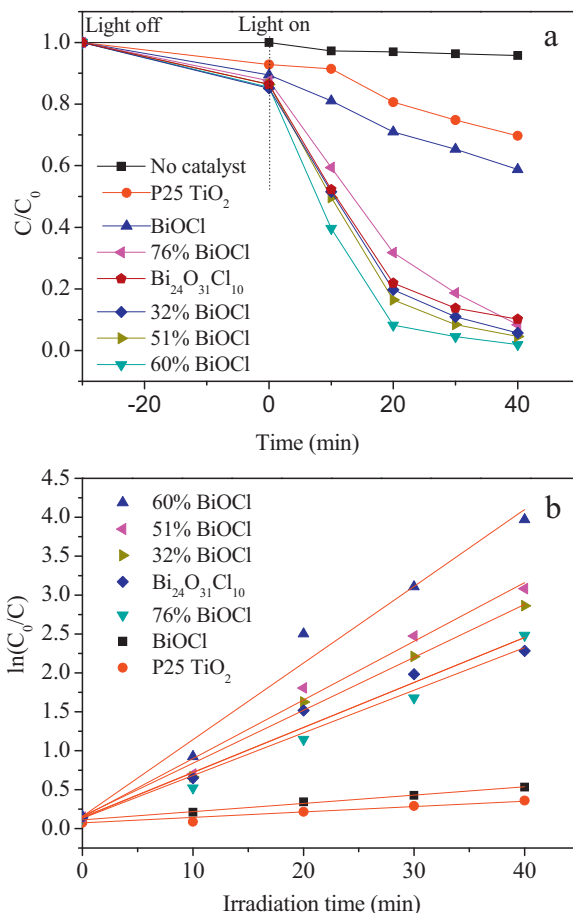


Fig. 6. Time-course variation of (a) C/C_0 and (b) $\ln(C_0/C)$ of RhB solution under visible light illumination over various catalysts.

the decoloration of MO and RhB over the catalysts. First, the as-prepared BiOCl and P25 TiO_2 exhibit photoactivities on RhB to some extent, which can be attributed to the photosensitization; however there is almost no photosensitization for MO. Second, although the photocatalytic activity order of various photocatalysts for degradation of RhB is different from that of MO because of the existence of sensitization, the 60%BiOCl composite also shows the highest activity. Third, it is interesting that the photocatalysts depict excellent adsorption performance for RhB, which may be related to the surface charge of materials. As representation, the zeta potentials of the 60%BiOCl photocatalyst under different pH conditions were measured and the results are shown in Fig. 7. The results indicated that the as-prepared 60%BiOCl possessed surface negative charges ($\zeta = -16.8 \text{ mV}$) at neutral condition. This feature may explain the good adsorption ability of the cationic dye to the composite samples. It is also

Table 2

The pseudo-first order rate constants k for MO photocomposition over various catalysts.

Sample	Fitted equation	$k \text{ (min}^{-1}\text{)}$	Correlation coefficient R
BiOCl	$y = 0.0025x + 0.0677$	0.0025	0.9849
76%BiOCl	$y = 0.0044x + 0.0557$	0.0044	0.9772
60%BiOCl	$y = 0.0135x + 0.0618$	0.0135	0.9920
51%BiOCl	$y = 0.0075x + 0.0786$	0.0075	0.9902
32%BiOCl	$y = 0.0081x + 0.0572$	0.0081	0.9976
$\text{Bi}_{24}\text{O}_{31}\text{Cl}_{10}$	$y = 0.0037x + 0.0158$	0.0037	0.9975
P25 TiO_2	$y = 0.0001x + 0.0423$	0.0001	0.9873

Table 3

The pseudo-first order rate constants k for RhB photocomposition over various catalysts.

Sample	Fitted equation	$k \text{ (min}^{-1}\text{)}$	Correlation coefficient R
BiOCl	$y = 0.0106x + 0.1111$	0.0106	0.9978
76%BiOCl	$y = 0.0548x + 0.1331$	0.0548	0.9903
60%BiOCl	$y = 0.0985x + 0.1568$	0.0985	0.9896
51%BiOCl	$y = 0.0753x + 0.1461$	0.0753	0.9937
32%BiOCl	$y = 0.0679x + 0.1612$	0.0679	0.9955
$\text{Bi}_{24}\text{O}_{31}\text{Cl}_{10}$	$y = 0.0579x + 0.1399$	0.0579	0.9853
P25 TiO_2	$y = 0.007x + 0.0744$	0.007	0.9749

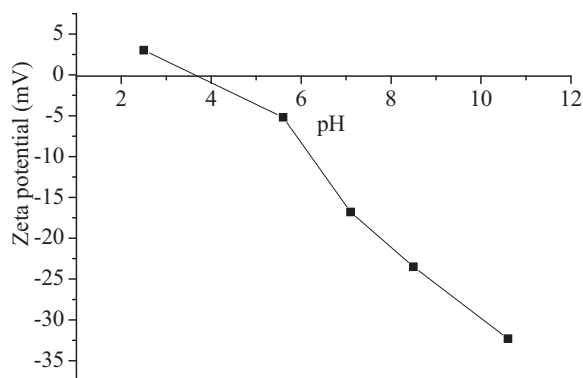


Fig. 7. Zeta potential of 60%BiOCl as a function of solution pH.

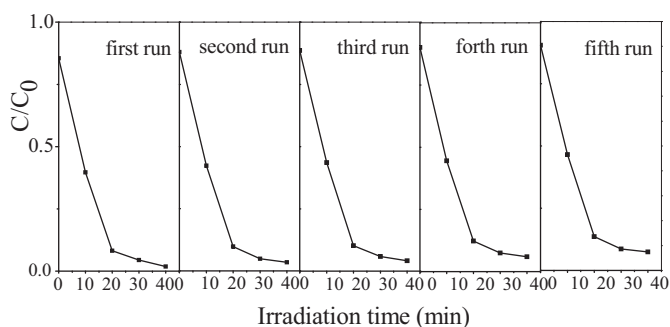


Fig. 8. Cycling runs in the photocatalytic degradation of RhB with sample 60%BiOCl under visible light irradiation.

deduced that the isoelectric point of 60%BiOCl is approximately 3.7.

To observe its stability under light irradiation, the recycling result is shown in Fig. 8 using 60%BiOCl sample. The degradation rate of RhB decreases from 98.1% to 92.5% at 40 min after five run, showing that there is only little loss of activity. The XRD patterns of 60%BiOCl sample before and after reaction are shown in Fig. 9. It is seen that although peak intensity decreases slightly for used sample because of the loss of some nanoparticles during the separation process, the ratio of the two components remains steadiness, indicating that the as-prepared heterojunctions are stable during irradiation.

RhB and MO are typical dyes. To observe the universality of the as-prepared heterojunctions, the degradation results of 4-CP are shown in Fig. 10. After 4 h of irradiation, the removal yield of 4-CP is 88.2%, showing the efficient ability of the heterojunctions in the degradation of refractory organic compounds.

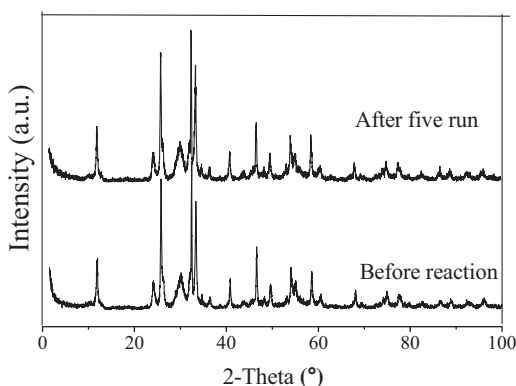


Fig. 9. XRD patterns of 60%BiOCl sample before and after reaction.

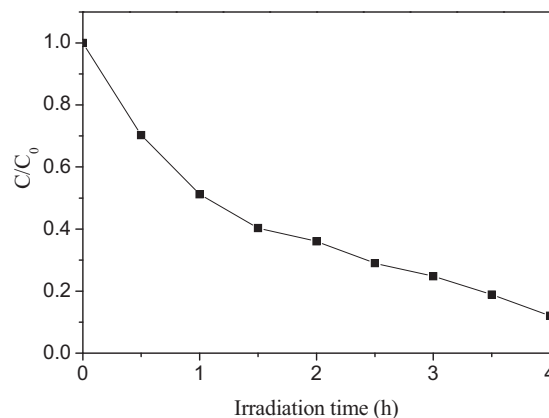


Fig. 10. Time-course variation of C/C_0 of 4-CP solution under visible light illumination over 60%BiOCl.

3.4. Photocatalytic mechanism

3.4.1. Active species detection

To detect the main active oxidative species responsible for the degradation in the photocatalytic process, the influence of some radical scavengers and N_2 purging on the degradation of MO over 60%BiOCl under visible light irradiation was investigated. As shown in Fig. 11, the photocatalytic degradation efficiencies of MO significantly decreased in the presence of 1 mM ammonium oxalate monohydrate ($(NH_4)_2C_2O_4 \cdot H_2O$, h^+ scavenger) [37], showing h^+ is the main reactive species.

On the other hand, it is known that benzoquinone (BQ) is an effective $\bullet O_2^-$ scavenger and is widely used to detect the existence of $\bullet O_2^-$. However, in this study, when BQ was added into the photocatalytic reaction system, the solution became black, which indicates there is reaction occurred between BQ and pollutant or photocatalyst. This phenomenon cannot be explained by us now and should be further studied. To illustrate the role of $\bullet O_2^-$ radical, $AgNO_3$ (e^- scavenger) [38] and N_2 purging were taken to replace BQ. It is seen that the addition of $AgNO_3$ improves the degradation of MO because the capture of electrons by $AgNO_3$ enhances the separation efficiency of photo-generated electrons and holes and more holes move to the surface of catalyst to react with MO molecules. It indicates that the role of $\bullet O_2^-$ is less than that of h^+ because $\bullet O_2^-$ is derived from e^- and O_2 . Meanwhile, N_2 purging decreases the degradation efficiency of MO, showing O_2 has certain effect in the degradation of MO and $\bullet O_2^-$ is also a kind of reactive species. On

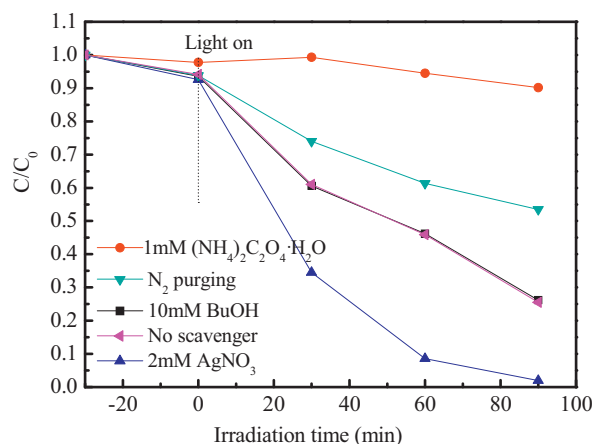


Fig. 11. Time course of the photodegradation of MO over the as-prepared 60%BiOCl photocatalyst in the presence of various radicals scavengers.

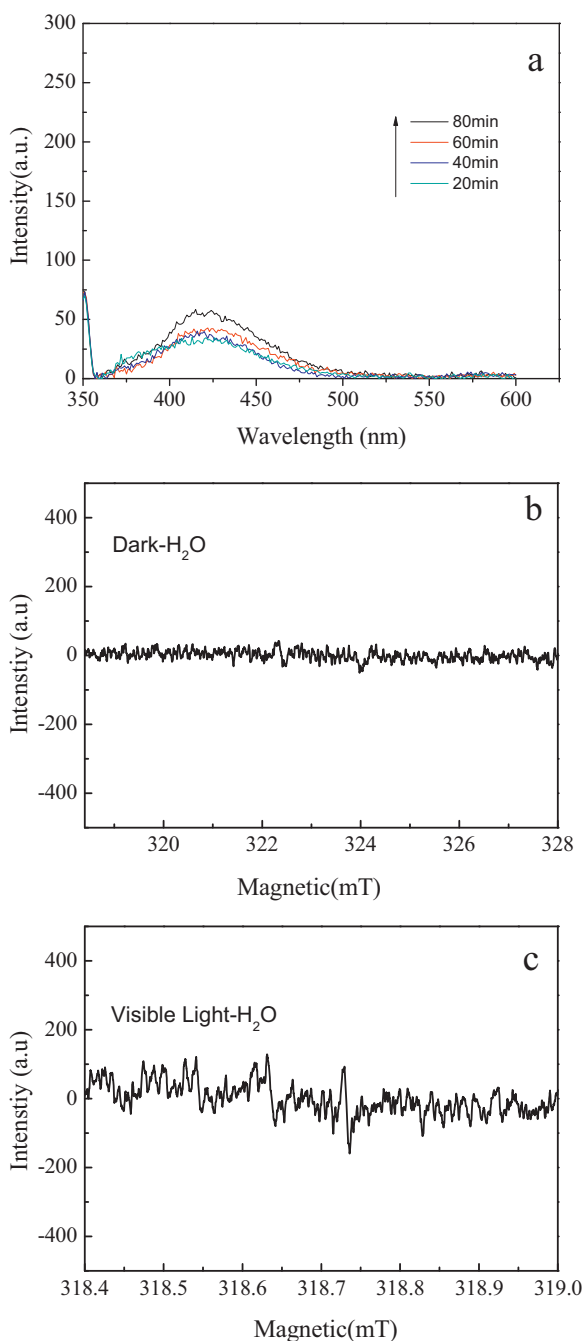


Fig. 12. (a) OH-trapping fluorescence spectra of 60%BiOCl sample in a TA solution under visible (excitation at 315 nm, emission at 425 nm), and DMPO spin-trapping ESR spectrum over 60%BiOCl in aqueous dispersion for DMPO-•OH (b) in dark, (c) under visible light irradiation.

the other hand, *t*-BuOH as •OH scavenger [39] has no any effect on the photo-degradation of MO. The results suggest that there is no •OH radical generated in the photocatalytic process.

To further investigate whether there are •OH radicals in detail, the TAOH fluorescence and ESR method were employed as shown in Fig. 12. It is seen from Fig. 12a that the fluorescence signals are very weak and with the increase of time there is almost no improvement of peak intensity, indicating that •OH radicals are not involved in the photodegradation process. The fluorescence peaks of little •OH radicals observed may be generated from the •O₂⁻ radicals. Fig. 12b and c shows DMPO-•OH signals in dark and under visible

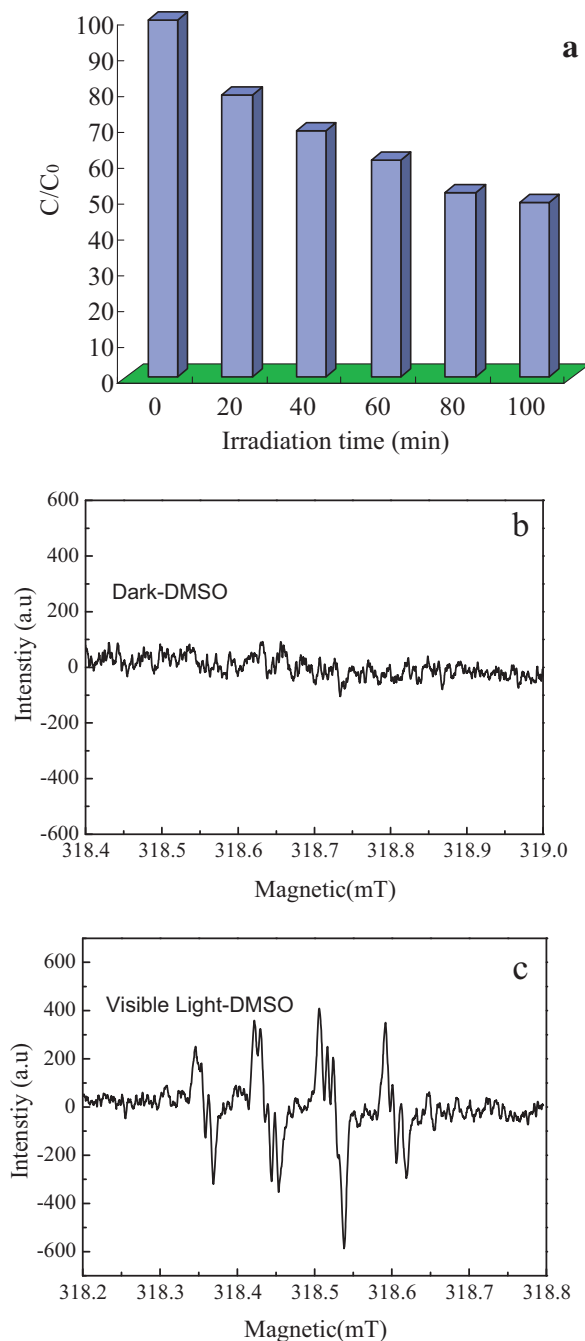
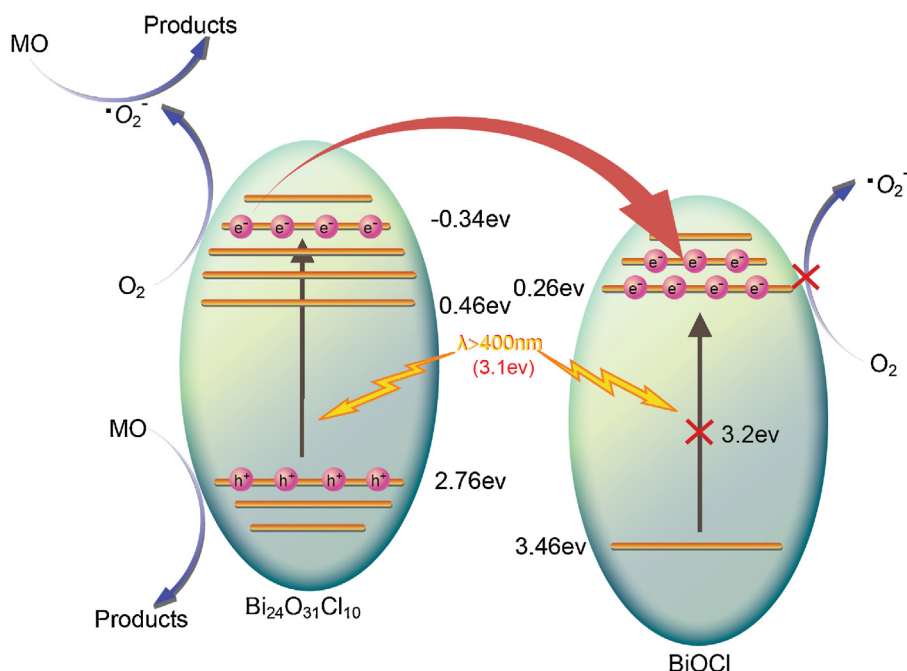


Fig. 13. (a) Time course of transformation percentage of NBT concentration over 60%BiOCl heterojunction, and DMPO spin-trapping ESR spectrum over 60%BiOCl in DMSO solvent for DMPO-•O₂⁻ (b) in dark, (c) under visible light irradiation.

light irradiation, respectively. It is seen that nearly no •OH signals can be detected, which is consistent with the TAOH result.

From the theoretical viewpoint, it is almost impossible for the production of •OH in the Bi-based photocatalysts system. Generally, in a valence band of Bi³⁺, holes formed by photoexcitation are regarded as Bi⁵⁺ or Bi⁴⁺ [40]. The standard redox potential of Bi₂O₄/BiO⁺ (Bi^V/Bi^{III}) ($E^\circ = +1.59$ eV at pH 0) in aqueous solution [41] can make sense for a rough estimation of the oxidation potential of hole (Bi⁵⁺) photogenerated in the Bi-based photocatalyst, which is more negative than that of •OH/H₂O (+2.27 eV versus the standard hydrogen electrode (SHE)) [42] and •OH/OH⁻ (+1.99 eV) [43]. Therefore, the holes photo-generated on the surface of the



Scheme 1. Schematic illustration of the charge separation and transfer in the BiOCl/Bi₂₄O₃₁Cl₁₀ heterojunctions under visible-light irradiation.

as-prepared BiOCl/Bi₂₄O₃₁Cl₁₀ cannot react with H₂O/OH[−] to form •OH.

To observe the generation of •O₂[−] in detail, NBT was used to determine the amount of •O₂[−] generated from the obtained 60%BiOCl heterojunction photocatalytic system. Fig. 13a shows the time course of transformation percentage of NBT over 60%BiOCl sample. It is obvious that the transformation percentage of NBT increases with the irradiation time due to the reaction between •O₂[−] and NBT, illustrating that electrons can react with O₂ to produce •O₂[−]. Furthermore, the DMPO-•O₂[−] signals shown in Fig. 13b and c with dimethyl sulphoxide (DMSO) as solvent instead of water further prove the existence of •O₂[−] [44]. It can be seen that no signals can be detected without irradiation and the •O₂[−] radicals can be produced over the 60%BiOCl heterojunction under visible light irradiation. It is also interesting that besides the •O₂[−] radicals signal, there is also impurity signal, which may be attributed to the chlorine or other radicals and should be investigated in the future.

3.4.2. Band gap structures and electrons transfer route

It is important to determine the relative conduction band (CB) and valence band (VB) potentials of the semiconductors composing heterojunction for the investigation of photo-induced carriers transfer route. The band edge positions of BiOCl and Bi₂₄O₃₁Cl₁₀ can be theoretically calculated using the atom's Mulliken electronegativity equation [45,46].

$$E_{VB} = \chi - E^e + 1/2E_g \quad (3)$$

where χ is the electronegativity of semiconductor, E^e is the energy of free electrons on the hydrogen scale (≈ 4.5 eV), E_g is the band gap energy of semiconductor; and E_{CB} can be calculated by $E_{CB} = E_{VB} - E_g$. Table 4 lists the electronegativities, the calculated CB and VB potentials of BiOCl and Bi₂₄O₃₁Cl₁₀ using equations as mentioned above.

However, it is known that the standard redox potential of O₂/•O₂[−] is -0.284 eV, which is more negative than the CB potentials of BiOCl (0.26 eV) and Bi₂₄O₃₁Cl₁₀ (0.46 eV). That is, it is impossible to generate •O₂[−] radicals in this photocatalytic system, which is conflict to the results of scavenger, NBT, and ESR. Then, where are the •O₂[−] radicals from?

In this research, the wavelength of 400 nm corresponds to energy of 3.1 eV, which is larger than the E_g of Bi₂₄O₃₁Cl₁₀ and smaller than that of BiOCl. Therefore, the electrons on the VB of BiOCl cannot be activated; however, in the case of Bi₂₄O₃₁Cl₁₀, the electrons can be excited from the VB at 2.76 eV position to a higher potential edge of -0.39 eV. Accordingly, the new CB potential of Bi₂₄O₃₁Cl₁₀ (-0.39 eV) is more negative than that of $E(O_2/\bullet O_2^-)$ (-0.284 eV). As a consequence, photogenerated electrons on this position can react with O₂ to form •O₂[−] radicals. Meanwhile, some electrons can also migrate easily to the CB (0.26 eV) of BiOCl via the interfaces in the system. In this way, the BiOCl/Bi₂₄O₃₁Cl₁₀ composites can efficiently decrease the undesired recombination of photogenerated holes and electrons, and more holes can react with pollutants to enhance the photodegradation efficiency [36]. It should be mentioned that the transferred electrons on the BiOCl CB edge below -0.284 eV can not react with O₂, except for the electrons locating the potential higher than -0.284 eV.

To observe the separation efficiency of electron-hole pair, surface photovoltage measurement was employed. Generally, the higher the SPV signal, the higher the separation rate of photoinduced charge carriers is [47,48]. Fig. 14 reflects the SPS responses of pristine BiOCl, Bi₂₄O₃₁Cl₁₀, and 60%BiOCl composite as representative for heterojunctions. For BiOCl and Bi₂₄O₃₁Cl₁₀, the obvious SPS peaks appear at about 327 and 375 nm, respectively, which can be attributed mainly to the electron transition from their VB to CB on the basis of band structure [47]. Furthermore, there is also an obvious response for Bi₂₄O₃₁Cl₁₀ in visible light region, showing its narrow band gap. For 60%BiOCl heterojunction, there are mainly two responses at about 340 and 415 nm, which are contributed by BiOCl and Bi₂₄O₃₁Cl₁₀ respectively. The obvious enhanced SPS

Table 4

Electronegativity, calculated CB and VB edge positions of BiOCl and Bi₂₄O₃₁Cl₁₀ semiconductor.

Semiconductor	Electronegativity (χ)(eV)	Calculated CB position (eV)	Calculated VB position (eV)
BiOCl	6.36	0.26	3.46
Bi ₂₄ O ₃₁ Cl ₁₀	6.11	0.46	2.76

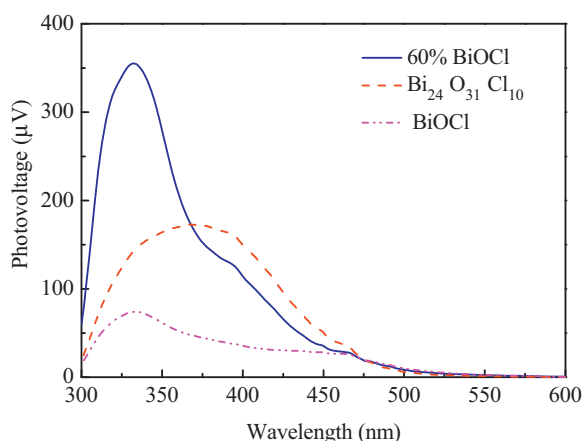


Fig. 14. SPS responses of various as-prepared samples.

response of 60%BiOCl sample indicates that the heterostructure greatly increases the separation efficiency of photogenerated electrons and holes.

On the basis of the above results and analysis, a possible pathway for the photodegradation of MO over BiOCl/Bi₂₄O₃₁Cl₁₀ heterojunctions under visible light ($\lambda > 400$ nm) is proposed as Scheme 1. First, electrons in the VB of Bi₂₄O₃₁Cl₁₀ with narrow band gap are excited to the high CB potential (−0.34 eV) under visible light irradiation. Some of them would be trapped by O₂ adsorbed on the surface of photocatalyst particles to form •O₂[−] radicals; some transfer to the CB BiOCl, leaving photogenerated holes on the VB of Bi₂₄O₃₁Cl₁₀. Then the MO would react with the photogenerated holes and subsequently be degraded. In this photocatalytic process, holes on the VB of Bi₂₄O₃₁Cl₁₀ cannot react with H₂O or OH[−] adsorbed on the surface of catalyst to generate •OH radicals.

4. Conclusions

BiOCl/Bi₂₄O₃₁Cl₁₀ heterojunctions have been developed for the first time by the self-combustion of ionic liquids using (C₂H₅)₂NH·HCl as cation of the ionic liquids and the main fuel in for the combustion and urea as the assistant fuel. The ratio of BiOCl to Bi₂₄O₃₁Cl₁₀ can be adjusted by varying the ratio of (C₂H₅)₂NH·HCl and urea because they contain different content of chlorine and oxygen. The band gaps of pristine BiOCl and Bi₂₄O₃₁Cl₁₀ are 3.2 and 2.3 eV, respectively. The prepared heterojunctions show noticeable visible light photocatalytic activity using anionic dye methyl orange and cationic dye rhodamine B as objective pollutants. The CB and VB positions of BiOCl and Bi₂₄O₃₁Cl₁₀ are calculated by atom's Mulliken electronegativity equation. Under visible light ($\lambda > 400$ nm, corresponding to a band gap of 3.1 eV) irradiation, electrons are activated from VB (2.76 eV) to a high CB position (−0.34 eV) of Bi₂₄O₃₁Cl₁₀. Some of these electrons transfer to the CB (0.26 eV) of BiOCl; some react with O₂ to generate •O₂[−] radicals, which are involved in the photocatalytic process. On the other hand, the left holes in the VB of Bi₂₄O₃₁Cl₁₀ are the main reactive species for the photodegradation of pollutants. The heterojunction containing 60.4% BiOCl and 39.6% Bi₂₄O₃₁Cl₁₀ shows the highest photocatalytic activity. Furthermore, the heterojunctions obtained possess surface negative charges, which is benefit to the adsorption for the cationic dyes.

Acknowledgment

This work was supported by the National Natural Science Foundation of China (No. 21076060, 21376061), and the Program for New Century Excellent Talents in University (No. NCET-12-0686),

and the One-Hundred Outstanding Innovative Talents Scheme of Hebei Province Education Department (No. CPRC022).

References

- [1] K.L. Zhang, C.M. Liu, F.Q. Huang, C. Zheng, W.D. Wang, *Applied Catalysis B: Environmental* 68 (2006) 125–129.
- [2] X.X. Li, J. Zhao, J.L. Yang, *Scientific Reports* 3 (2013) 1858.
- [3] H. Yamashita, Y. Fujii, Y. Ichihashi, S.G. Zhang, K. Ikeue, D.R. Park, K. Koyano, T. Tatsumi, M. Anpo, *Catalysis Today* 45 (1998) 221–227.
- [4] D. Ravelli, D. Dondi, M. Fagnoni, A. Albini, *Chemical Society Reviews* 38 (2009) 1999–2011.
- [5] J. Andersen, M. Pelaez, L. Guay, Z.H. Zhang, K. O'Shea, D.D. Dionysiou, *Journal of Hazardous Materials* 260 (2013) 569–575.
- [6] X. Xiao, R.P. Hu, C. Liu, C.L. Xing, X.X. Zuo, J.M. Nan, L.S. Wang, *Chemical Engineering Journal* 225 (2013) 790–797.
- [7] F.T. Li, Y. Zhao, Y.J. Hao, X.J. Wang, R.H. Liu, D.S. Zhao, D.M. Chen, *Journal of Hazardous Materials* 239–240 (2012) 118–127.
- [8] S. Cong, Y.M. Xu, *Journal of Physical Chemistry C* 115 (2011) 21161–21168.
- [9] A.D. Paola, E. García-López, G. Marci, L. Palmisano, *Journal of Hazardous Materials* 211–212 (2012) 3–29.
- [10] S. Shenawi-Khalil, V. Uvarov, E. Menes, I. Popov, Y. Sasson, *Applied Catalysis A: General* 413–414 (2012) 1–9.
- [11] X.B. Chen, S.S. Mao, *Chemical Reviews* 107 (2007) 2891–2959.
- [12] K. Fukui, T. Kamegawa, K. Mori, H. Yamashita, *Chemistry—An Asian Journal* 7 (2012) 1366–1371.
- [13] A. Vijayabalan, K. Selvam, R. Velmurugan, M. Swaminathan, *Journal of Hazardous Materials* 172 (2009) 914–921.
- [14] C.H. Wang, C.L. Shao, Y.C. Liu, L. Zhang, *Scripta Materialia* 59 (2008) 332–335.
- [15] Y.Q. Lei, G.H. Wang, S.Y. Song, W.Q. Fan, H.J. Zhang, *CrystEngComm* 11 (2009) 1857–1862.
- [16] S.J. Wu, C. Wang, Y.F. Cui, T.M. Wang, B.B. Huang, X.Y. Zhang, X.Y. Qin, *Materials Letters* 64 (2010) 115–118.
- [17] B. Sarwan, B. Pare, A.D. Acharya, S.B. Jonnalagadda, *Journal of Photochemistry and Photobiology B: Biology* 116 (2012) 48–55.
- [18] S.J. Peng, L.L. Li, P.N. Zhu, Y.Z. Wu, M. Srinivasan, S.G. Mhaisalkar, S. Ramakrishna, Q.Y. Yan, *Chemistry—An Asian Journal* 8 (2013) 258–268.
- [19] X. Xiao, R. Hao, M. Liang, X.X. Zuo, J.M. Nan, L.S. Li, W.D. Zhang, *Journal of Hazardous Materials* 233–234 (2012) 122–130.
- [20] F. Dong, Y.J. Sun, M. Fu, Z.B. Wu, S.C. Lee, *Journal of Hazardous Materials* 219–220 (2012) 26–34.
- [21] J. Cao, B.Y. Xu, H.L. Lin, B.D. Luo, S.F. Chen, *Catalysis Communications* 26 (2012) 204–208.
- [22] H.F. Cheng, B.B. Huang, X.Y. Qin, X.Y. Zhang, Y. Dai, *Catalysis Communications* 48 (2012) 97–99.
- [23] S.Y. Chai, Y.J. Kim, M.H. Jung, A.K. Chakraborty, D. Jung, W.I. Lee, *Journal of Catalysis* 262 (2009) 144–149.
- [24] S. Shamaila, A.K.L. Sajjad, F. Chen, J.L. Zhang, *Journal of Colloid and Interface Science* 356 (2011) 465–472.
- [25] X.F. Chang, G. Yu, J. Huang, Z. Li, S.F. Zhu, P.F. Yu, C. Cheng, S.B. Deng, G.B. Ji, *Catalysis Today* 153 (2010) 193–199.
- [26] J. Zhang, J.X. Xia, S. Yin, H.M. Li, H. Xu, M.Q. He, L.Y. Huang, Q. Zhang, *Colloids and Surfaces A—Physicochemical and Engineering Aspects* 420 (2013) 89–95.
- [27] K. Rajeshwar, N.R. de Tacconi, *Chemical Society Reviews* 38 (2009) 1984–1998.
- [28] F.T. Li, Y. Liu, Z.M. Sun, R.H. Liu, C.G. Kou, Y. Zhao, D.S. Zhao, *Materials Letters* 65 (2011) 406–408.
- [29] G.K. Pradhan, S. Martha, K.M. Parida, *ACS Applied Materials & Interfaces* 4 (2012) 707–713.
- [30] F.T. Li, Y. Liu, Z.M. Sun, Y. Zhao, R.H. Liu, L.J. Chen, D.S. Zhao, *Catalysis Science & Technology* 2 (2012) 1455–1462.
- [31] U. Eggenweiler, E. Keller, V. Kraemer, *Acta Crystallographica Section B—Structural Science* 56 (2000) 431–437.
- [32] L.Q. Ye, J.Y. Liu, Z. Jiang, T.Y. Peng, L. Zan, *Applied Catalysis B: Environmental* 142–143 (2013) 1–7.
- [33] K.I. Ishibashi, A. Fujishima, T. Watanabe, K. Hashimoto, *Electrochemistry Communications* 2 (2000) 207–210.
- [34] O. Xiao, Z.C. Si, J. Zhang, C. Xiao, X.K. Tan, *Journal of Hazardous Materials* 150 (2008) 62–67.
- [35] J. Cao, B.D. Luo, H.L. Lin, B.Y. Xu, S.F. Chen, *Applied Catalysis B: Environmental* 111–112 (2012) 288–296.
- [36] T.B. Li, G. Chen, C. Zhou, Z.Y. Shen, R.C. Jin, J.X. Sun, *Dalton Transactions* 40 (2011) 6751–6758.
- [37] S.J. Liang, R.W. Liang, L.R. Wen, R.S. Yuan, L. Wu, X.X. Fu, *Applied Catalysis B: Environmental* 125 (2012) 103–110.
- [38] Y.J. Wang, R. Shi, J. Lin, Y.F. Zhu, *Energy Environmental Science* 4 (2011) 2922–2929.
- [39] F.T. Li, X.J. Wang, Y. Zhao, J.X. Liu, Y.J. Hao, R.H. Liu, D.S. Zhao, *Applied Catalysis B: Environmental* 144 (2014) 442–453.
- [40] H.B. Fu, C.S. Pan, W.Q. Yao, Y.F. Zhu, *Journal of Physical Chemistry B* 109 (2005) 22432–22439.
- [41] R.C. Weast, *Handbook of Chemistry and Physics*, CRC Press, Boca Raton, FL, 1988.

- [42] A. Fujishima, X.T. Zhang, *Comptes Rendus Chimie* 9 (2006) 750–760.
- [43] S. Kim, W. Choi, *Environmental Science & Technology* 36 (2002) 2019–2025.
- [44] X.J. Bai, L. Wang, R.L. Zong, Y.F. Zhu, *Journal of Physical Chemistry C* 117 (2013) 9952–9961.
- [45] A.H. Nethercot, *Physical Review Letters* 33 (1974) 1088–1091.
- [46] M.A. Butler, D.S. Ginley, *Journal of the Electrochemical Society* 125 (1978) 228–232.
- [47] L.Q. Jing, H.G. Fu, B.Q. Wang, D.J. Wang, B.F. Xin, S.D. Li, J.Z. Sun, *Applied Catalysis B: Environmental* 62 (2006) 282–291.
- [48] Y.C. Lu, Y.H. Lin, T.F. Xie, S.L. Shi, H.M. Fan, D.J. Wang, *Nanoscale* 4 (2012) 6393–6400.